

Article

Electron-Beam Processing of Aluminum-Containing Ceramics in the Forevacuum Pressure Range

Aleksandr Klimov , Ilya Bakeev  and Aleksey Zenin

Laboratory of Plasma Electronics, Tomsk State University of Control Systems and Radioelectronics, Tomsk 634050, Russia; bakeeviyu@mail.ru (I.B.); zenin1988@gmail.com (A.Z.)

* Correspondence: klimov@main.tusur.ru

Abstract: Aluminum–ceramic materials based on Al_2O_3 and AlN are widely used in the electronics industry and, according to a number of electrophysical and technical and economic parameters, are among the most suitable for the production of electrical and radio engineering products. In this study, it is shown that the treatment of ceramics based on Al_2O_3 with an electron beam with a power of 200–1100 W and a current of 10–50 mA leads to heating of the ceramic surface to a temperature of 1700 °C. When heated to a temperature of 1500 °C and kept at this temperature for no more than 10 s, an increase in the roughness of the ceramic surface is observed by more than an order of magnitude. At the same time, for ceramic substrates based on aluminum nitride, an increase in the temperature of electron beam treatment from 1300 to 1700 °C leads to an increase in thermal conductivity from 1.5 to 2 times. The edge angle of water wetting of the AlN surface can vary from 20 to 100 degrees depending on the processing temperature, which allows one to control the transition of the material from a hydrophilic to a hydrophobic state. At the same time, electron beam exposure to Al_2O_3 does not change the wettability of this material so much. Electron beam processing in the forevacuum pressure region allows controlled changes in the electrophysical properties of ceramic materials based on Al_2O_3 and AlN .

Keywords: plasma-cathode electron source; electron-beam irradiation; roughness; microhardness; thermal conductivity; ceramics; processing; Al_2O_3 ; AlN



Citation: Klimov, A.; Bakeev, I.; Zenin, A. Electron-Beam Processing of Aluminum-Containing Ceramics in the Forevacuum Pressure Range. *Ceramics* **2023**, *6*, 2098–2116. <https://doi.org/10.3390/ceramics6040129>

Academic Editor: Narottam P. Bansal

Received: 11 August 2023
Revised: 17 October 2023
Accepted: 18 October 2023
Published: 23 October 2023



Copyright: © 2023 by the authors. Licensee MDPI, Basel, Switzerland. This article is an open access article distributed under the terms and conditions of the Creative Commons Attribution (CC BY) license (<https://creativecommons.org/licenses/by/4.0/>).

1. Introduction

Aluminum oxide Al_2O_3 and aluminum nitride AlN share a number of properties, such as high hardness and wear resistance, which make them suitable for producing tools, bearings, coatings, and other wear-resistant machine components [1–6]. These ceramic materials are widely used in various fields of engineering, such as electronics, optics, metallurgy, and biomedicine [7–10].

Methods used to fabricate Al_2O_3 and AlN ceramics can be divided into conventional and unconventional approaches. Conventional methods are based on sintering aluminum oxide or nitride powders at high temperature and pressure. These methods include hot pressing, hot isostatic pressing, sintering in an electric field, and activated sintering [11–14]. Unconventional methods are based on the synthesis of aluminum oxide or nitride from other aluminum compounds at low temperature and pressure. They include sol-gel processing [15], gas-phase processing, and self-propagating high-temperature synthesis [16–18]. To improve the ceramic properties, various additives can be included in the composition, such as CaO , SiO_2 , Y_2O_3 , ZrO_2 , and SiC , among others. The properties of the resulting material are determined in many ways by the purity of the material itself and the additives used, as well as by the regime and method of sintering. Currently, despite the multiplicity of methods and approaches, there is a need for a means of controlled modification of the surface properties of aluminum oxide or nitride ceramics after sintering.

Ceramic surfaces can be modified in various ways, including processing by ions and plasma [19], electron-beam irradiation [20–23], and laser radiation [24,25]. These methods

can modify the ceramic chemical or phase composition, its roughness, and other properties of the surface layer, and thus improve its physical [26], mechanical [27,28], optical [29], and electrical characteristics [30–33].

Electron-beam irradiation is an advanced method of modifying materials that makes it possible to change the surface structure, phase composition, mechanical, optical, and electrical properties [34]. The method employs a high-intensity high-energy electron beam of tens to hundreds of keV to irradiate the surface in a vacuum chamber. A variety of physical and chemical processes then take place: heating, melting, evaporation, ionization, excitation, scattering, diffusion, recombination, etc. [35,36]. Electron-beam processing can be used to improve the hardness, wear and corrosion resistance, and dielectric permeability of the Al₂O₃ ceramic. However, existing methods of electron-beam treatment are problematic in that they require providing a low pressure in the electron beam generation and transport regions, which poses the problem of removing the negative charge that accumulates on the irradiated non-conducting surface due to the electron beam itself.

One solution to this problem is the use of a pulsed beam mode that allows the irradiated surface to partially discharge between pulses. The periodic beam action has its own specific features: in the course of the exposure, the surface layer of the treated material melts and then re-crystallizes. This processing regime brings about intense thermal stress and leads to the formation of pores and cracks on the surface [37].

The use of forevacuum-pressure plasma-cathode electron sources is an alternative method that improves the efficiency and quality of electron-beam treatment. These sources are capable of forming electron beams at relatively high pressures, in the range 5–20 Pa. At these pressures, surface charging of the irradiated dielectric is nearly completely neutralized by the flux of positive ions from the plasma generated in the electron beam transport region (the “beam-plasma”) [38]. We have demonstrated, in prior work, the value of using forevacuum plasma-cathode electron sources for sintering, surface modification, ceramic welding, and evaporation [39–41].

In the work described here we have explored the influence of an electron-beam processing regime, in the forevacuum pressure range, on the surface structure, strength, and thermal properties of aluminum oxide and nitride ceramics.

2. Materials and Investigation Techniques

We used commercially available substrates of the Al₂O₃ ceramic (Policor, JSC Policor, Kineshma, Russia) and aluminum nitride AlN (INC-AN180, Xiamen Innovacera Advanced Materials Co., Ltd., Xiamen, China). These materials are widely used in the electronics industry and are characterized by stable composition and minimum impurity content. The samples were polished plates 20 × 12 mm in size and 1 mm thick. Parameters of the substrates under study are shown in Table 1.

Table 1. Substrate parameters [42–44].

Parameter	Policor (Al ₂ O ₃)	INC-AN180 (AlN)
Content, %	99.7	96
Density, g/cm ³	3.96	3.3
TCLE, 10 ^{−6} /°C	8	4.8
Thermal conductivity, W/m·K	30	160–180
Dielectric constant (at 20 °C)	9.45–9.95	9
tan δ, 10 ^{−4}	1	5
Melting point, °C	2072	2200

The structure and elemental composition of the substrate surfaces after electron-beam treatment were analyzed using a Hitachi S-3400N scanning electron microscope (Hitachi High-Tech, Tokyo, Japan) coupled to a Bruker X’Flash 5010 energy-dispersive analyzer (Bruker AXS Microanalysis, Karlsruhe, Germany). The elemental composition of the

original materials is shown in Table 2. The porosity of the non-irradiated substrates did not exceed 1%.

Table 2. Elemental composition of original (unirradiated) substrates, at%.

	Nitrogen	Oxygen	Aluminum	Yttrium
AlN	48.2	0.9	49.4	1.5
Al ₂ O ₃	-	59.7	40.3	-

Thermal conductivity was measured by the two-probe technique [45]. When measuring the conductivity, a constant voltage of maximum value 500 V was applied. The current was measured by an analog nano-ammeter.

The presence of yttrium oxide in the aluminum nitride ceramic is to ensure sintering. Sintering of dense aluminum nitride materials is known to be challenging due to oxygen impurities in the initial powder. Oxygen penetrates into the aluminum nitride network, creating aluminum vacancies and reducing the thermal conductivity of the material. To overcome this issue, Y₂O₃ is normally added to aluminum nitride ceramic in a weight proportion of 1–5%.

Surface SEM photographs of the original substrates are shown in Figure 1. There are visible point defects on the surface of the original samples, which may be directly related to the substrate manufacturing technology.

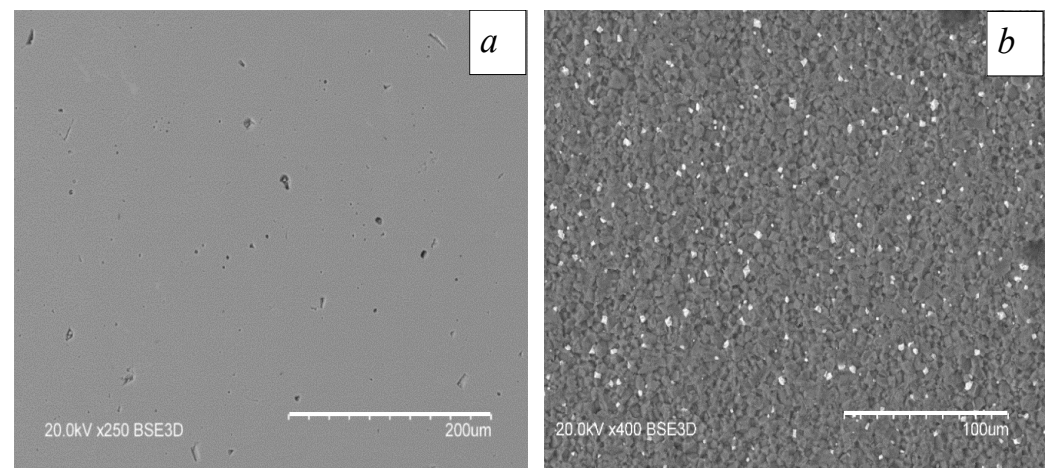


Figure 1. SEM surface images of original substrates: (a) Policor (Al₂O₃), (b) INC-AN180 (AlN).

The hardness was measured by the Vickers method, in which a tetrahedral pyramid is forced into the test sample under a specific load, using an HV5 Vickers Hardness Tester (Jinan Hensgrand Instrument Co., Jinan, China) with an overall measurement error of 10%.

Surface roughness was measured using a Micro Measure 3D Station (STIL, Aix En Provence, France) profilometer and a Mitutoyo SJ-210 (Mitutoyo Corporation, Takatsu-ku, Kawasaki, Japan) portable roughness tester with measurement accuracy of 5%.

Thermal conductivity was measured over the temperature range 10–500 °C in 100 °C steps in a monotonic heating mode using a PLK-1818 hot plate and a Fluke Ti2000 thermal imager (Everett, WA, USA) with a measurement accuracy of 5%. The temperature of the sample surface (T_S) and heating plate temperature (T_P) were measured under conditions close to equilibrium when thermal loss from side surfaces could be neglected.

The surface wettability with distilled water was determined according to the technique described in [46] using an MBS-10 (Rusoptics, Moscow, Russia) stereoscopic microscope with a magnification of 4× to 100× and equipment for determining the contact angle.

X-ray phase analysis (XPA) was carried out using an XRD7000S (Shimadzu, Kyoto, Japan) diffractometer. The diffraction patterns obtained were processed using the international PDF-2 database and the open-source software PowderCell 2.4.

3. Experimental Setup and Methods

Electron-beam treatment of ceramic surfaces was carried out on the experimental setup shown schematically in Figure 2. The setup includes a forevacuum-pressure plasma-cathode electron source, a 0.2 m³ vacuum chamber, vacuum pumping equipment based on a BocEdwads 80 M mechanical pump, electron beam power supplies, and diagnostic systems. The electron source, based on a hollow-cathode plasma, is mounted on a central flange of the vacuum chamber. The main parameters of the electron beam are beam current—up to 50 mA, electron beam energy—up to 15 keV, beam diameter at its focus (cross-over)—about 1 mm. Source design and parameters have been described in detail elsewhere [47]. The focusing magnetic field is capable of varying the beam diameter over the range 1 to 10 mm. The operating gas was helium (class A, 99.99% purity). The operating pressure at which the substrates were processed was 30 Pa. As our previous investigations have demonstrated, this pressure and inert gas are optimal for electron-beam treatment of non-conducting materials such as ceramics.

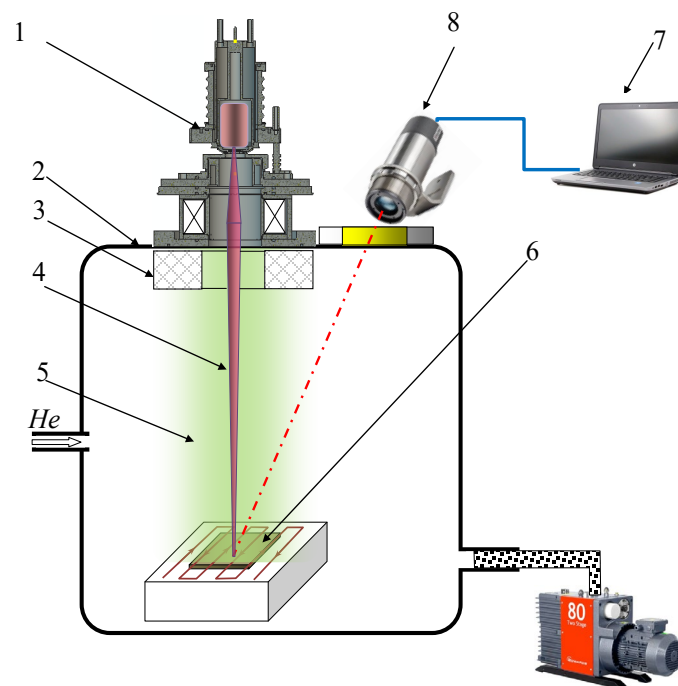


Figure 2. Schematic diagram of the experimental setup: 1—plasma-cathode electron source; 2—vacuum chamber; 3—beam deflection system; 4—electron beam; 5—beam-plasma; 6—sintered sample; 7—computer; 8—pyrometer.

The ceramic sample was placed on a crucible which was a flat bar made of graphite $20 \times 30 \times 10 \text{ mm}^3$ in size. The choice of graphite was because of its high heat resistance, capable of withstanding temperatures of several thousand degrees without deformation. To reduce the heat loss due to thermal conductivity, the crucible was suspended by tungsten wires (not shown in the figure). To ensure uniform irradiation of the substrate surface, the electron beam was raster-scanned over a rectangle of dimensions 1–2 mm greater than the substrate. During irradiation, the temperature variation over the substrate area did not exceed 15 °C. Focusing and deflection of the electron beam were carried out by magnetic coils located directly below the electron source extractor. The temperature time history during substrate processing is shown in Figure 3. The surface temperature increase was achieved by gradually increasing the beam current at a constant beam-accelerating voltage in the range 14–16 kV depending on the type of ceramic.

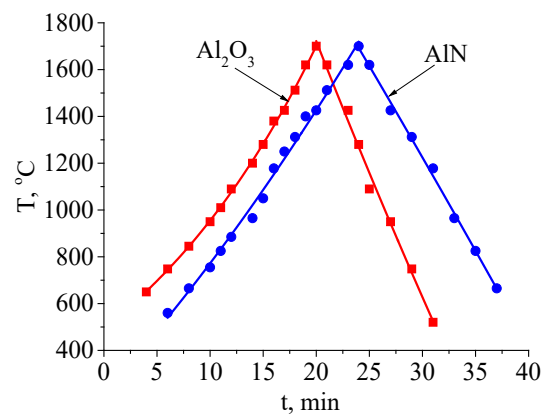


Figure 3. Thermal regime of electron-beam irradiation of samples. The holding temperature was 1700 °C.

The heating rate was 60–70 °C/min depending on the type of ceramic, the isothermal holding time was 10 s, and the cooling rate was 80 °C/min. The isothermal holding temperature of 1300–1700 °C with a discretization of 100 °C was selected so as to be in the range of 60–75% of the melting point. The overall time of electron-beam treatment was from 25 to 40 min, depending on the type of ceramic and the isothermal holding temperature. With increasing holding temperature, the overall processing time increased.

4. Results and Discussion

4.1. Electron-Beam Irradiation Regime

The types of ceramic used differ significantly in their thermal properties. Thus, Al₂O₃ has a lower melting point (2072 °C) than aluminum nitride AlN (2200 °C), which makes it more stable under thermal damage at high temperatures. However, the higher thermal conductivity of aluminum nitride (160–180 W/(m·K)) compared with that of aluminum oxide (30 W/(m·K)) makes it more efficient as a heat sink for heating elements and requires more energy to heat. During electron beam irradiation, the difference in thermal properties is fully manifested by the electron beam power needed to heat the Al₂O₃ and AlN surfaces to the required temperature. Figure 4 shows the substrate temperature dependence on electron beam power in the course of heating to the holding temperature. The dependencies are shown for two boundary temperatures, 1300 °C (black lines) and 1700 °C (blue lines). As can be seen, in order to heat aluminum oxide to a temperature of 1300 °C, it is necessary to increase the electron beam power to about 580 W (line 1), while heating aluminum nitride to the same temperature requires increasing the power by 140 W to a value of 720 W (line 2). At a temperature of 1700 °C, the difference in the beam power required to reach this temperature significantly increases. Thus, for the aluminum oxide ceramic, the electron beam power for heating to 1700 °C is 1120 W (line 3), while for the aluminum nitride ceramic, the required power is over 1600 W (line 4). In addition, a longer time is required for aluminum nitride to reach the desired temperature due to the need to increase the beam power by another 0.5 kW compared to the processing of aluminum oxide. Speeding up the heating process is not advisable due to possible damage to the irradiated substrate by strong thermomechanical stress.

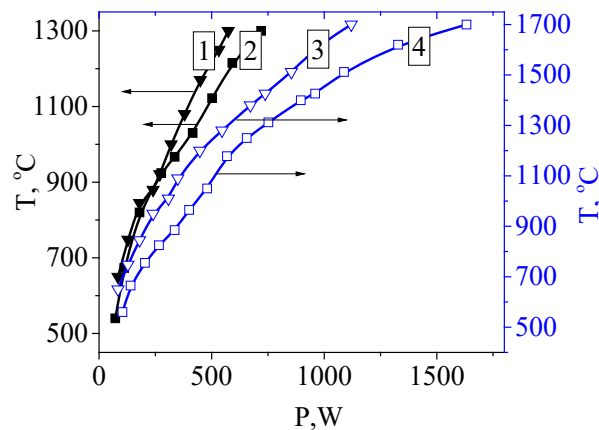


Figure 4. Dependence of sample temperature on electron beam power for different ceramics and holding temperatures: 1, 3—Al₂O₃; 2, 4—AlN.

4.2. Effect of Electron-Beam Treatment on the Surface of the Al₂O₃ Ceramic

In its original, unirradiated state, the Al₂O₃ substrate has a white color, as is characteristic of alumina ceramics. No grain structure appears on the surface of polished samples. After processing, the surface has a greyish tint. The change in color may testify to a broken stoichiometry of the composition in the surface layer inclined towards a shortage of oxygen. Depending on the surface temperature, the removal of oxygen from alumina ceramics is known to occur in a two-step manner: first through oxygen desorption from the surface, and then its release from the crystal lattice. The equation describing the dissociation reaction is [48,49]:



The conductivity of the ceramic samples was measured before and after electron-beam treatment. In measuring the conductivity of non-irradiated samples, the current through the measuring probes was recorded to the instrumentation accuracy (1 nA). No current was detected in samples after electron beam irradiation, which can be explained by the fact that the stoichiometric change in oxygen is insignificant due to the low processing temperature compared to the melting point. Indeed, according to [50,51], at 2350 °C, the density of free aluminum atoms in 100%-oxide alumina reaches 2.5%, however, a decrease in temperature to 2200 °C leads to a decrease in the oxygen content by an order of magnitude to 0.3%. With further decreases in temperature, one should expect a lower percentage of oxygen content in the surface layer.

Figure 5 shows SEM images of the surface after electron-beam irradiation of the aluminum oxide ceramic at different isothermal holding temperatures.

One can conclude from these images that electron-beam irradiation at a temperature of 1300 °C does not result in a significant change in surface structure. However, when the temperature rises to 1500 °C and above, melting occurs followed by re-crystallization of the ceramic surface layer and formation of micro blocks 50–100 μm in size, indicating texturization of the ceramic microstructure. Along with the micro-block boundaries, there are observed pores with an average size of 2–5 μm. At a surface temperature of 1700 °C, the micro-blocks form into regular cubic grains of size 100–150 μm, which is indicative of the formation of a new phase—the Al₂O₃ γ-phase (Figure 5d). The presence of pores in the surface layer is connected with the process of their creation and growth in a thin layer of the melt due to the presence of gas-forming elements, which can evaporate (mainly of oxygen, which is a ceramic constituent, and which is released during oxide dissociation). The presence of a melt layer on the surface of irradiated ceramics at a surface temperature below the melting point (2072 °C) is possible due to local melting of a thin layer under the focused electron beam. Due to peculiarities of the electron beam scanning and positioning system, the movement of the beam, though rather fast (the scanning frequency is 100 Hz), is yet discrete. During the short time when the beam stops, the surface may heat to a higher

temperature than the temperature of the whole surface measured by the pyrometer. The small average size of the pores formed after electron-beam irradiation is indicative of the short time of existence of the liquid phase in the surface layer and of rapid movement of the molten and solidified areas over the substrate surface. The formation of pores on the surface after re-crystallization is an undesirable effect, since pores are normally stress concentrators and facilitate cracking [52]. In our case, no cracking was detected, and only grain boundaries were more prominent.

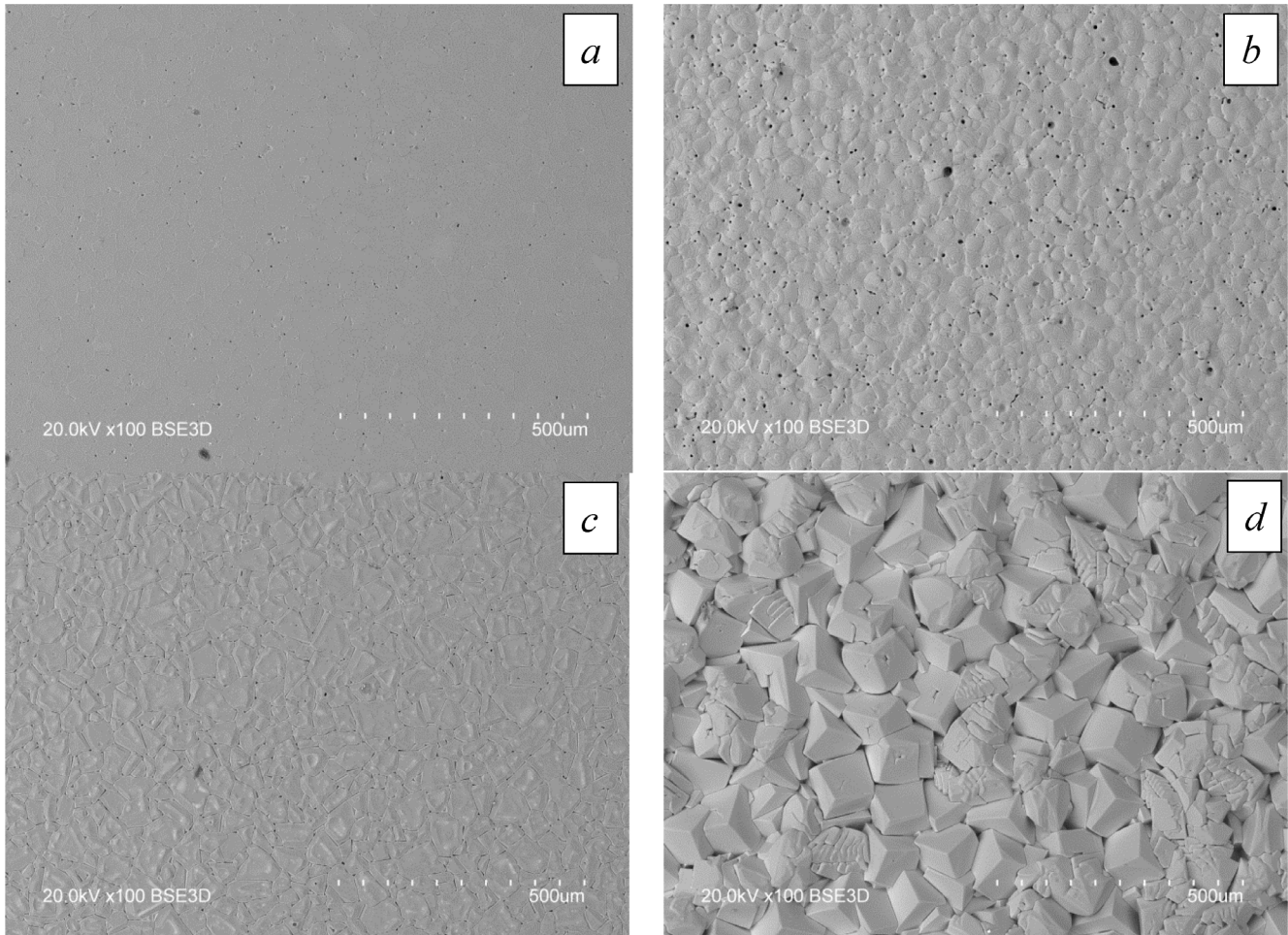


Figure 5. Surface of aluminum oxide ceramic samples processed at different holding temperatures: (a) 1300 °C, (b) 1500 °C, (c) 1600 °C, (d) 1700 °C.

Analysis of the elemental composition of irradiated Al_2O_3 ceramic samples shows that electron-beam irradiation in a helium atmosphere does not result in noticeable change in the surface layer elemental composition. Figure 6 shows typical profilograms of the relief of the surface areas of Al_2O_3 ceramic in its original state and after irradiation at a temperature of 1300 °C, 1400 °C, 1500 °C, and 1600 °C. The horizontal axis in Figure 6 indicates the length in mm over which the surface roughness was measured and the vertical axis indicates the roughness parameter R_a which is an arithmetic mean of absolute values of profile deviations within the base length. Thus, the surface roughness parameter is $R_{a0} = 0.0258 \mu\text{m}$ for the original sample, $R_{a1300} = 0.150 \mu\text{m}$ for the sample processed at 1300 °C, and $R_{a1500} = 2.93 \mu\text{m}$ for the sample processed at 1500 °C.

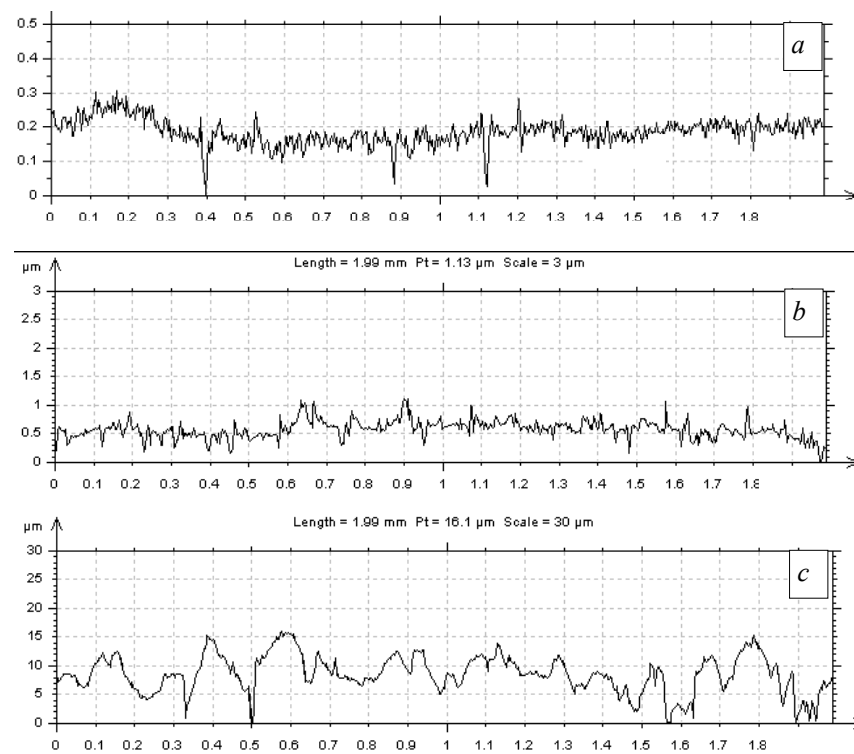


Figure 6. Roughness of Al_2O_3 ceramics: (a) original sample; (b) irradiated at $1300\text{ }^\circ\text{C}$; (c) irradiated at $1500\text{ }^\circ\text{C}$.

As can be seen, with an increase in surface temperature, the roughness increases by several factors. However, when the temperature reaches $1600\text{ }^\circ\text{C}$, the irregularities decrease and the substrate surface levels out. With further increases in temperature, the roughness parameter continues to grow and reaches a maximum, as is confirmed by the SEM images, Figure 5d. The increase in roughness is primarily connected with the fact that the electron beam energy introduced into the sample is spent on melting the surface layer, which upon cessation of irradiation undergoes rapid re-crystallization, leading to grain growth with the formations of surface protrusions that negatively affect surface roughness (Figure 6b). A further increase in processing temperature leads to significant growth of aluminum oxide grains in the form of elongated rectangles and cubes.

Change in the surface structure brings about change in the ceramic strength properties. Table 3 shows the results of measurements of microhardness by the Vickers method, which is based on denting a tetrahedral pyramid with an angle of 136° at the apex between opposite faces under a load; here the load was 5 kg. The data are given in the HV5 scale.

Table 3. Substrate microhardness measured by the Vickers method.

Processing Regime	HV5
Original	1700
$1300\text{ }^\circ\text{C}$	1620
$1400\text{ }^\circ\text{C}$	1600
$1500\text{ }^\circ\text{C}$	1580
$1600\text{ }^\circ\text{C}$	1510
$1700\text{ }^\circ\text{C}$	-

For the sample processed at a temperature of $1700\text{ }^\circ\text{C}$, the hardness was not measured because it was not possible to find a flat area on the surface suitable for measurement. Omitting this sample, one can see that the hardness tends to decrease with increasing isothermal holding temperature.

4.3. Effect of Electron-Beam Treatment on the Surface of the AlN Ceramic

As already mentioned, AlN, being a highly thermally conducting and non-toxic ceramic material, is in great demand by the electronics industry. As for the majority of ceramic materials, the purity of the original powder, the sintering mode, and the additives used play decisive roles in fabricating ceramics with the required properties after sintering. Also, the thermal conductivity properties of aluminum nitride depend on the conditions under which the sintered material is processed [53].

Figure 7 shows SEM images of the surfaces of AlN substrates processed at different temperatures. The white inclusions in Figure 7a–c are particles of yttrium aluminate, which is formed during the sintering of aluminum nitride ceramic. The covalent nature of the Al–N bond requires high sintering temperatures. Due to the presence of oxygen impurity in the original powder, oxygen penetrates into the nitride aluminum lattice during sintering and creates aluminum vacancies, which results in the scattering of phonons, and therefore in a decrease in thermal conductivity of the material. When an yttrium oxide additive is used, it interacts with Al_2O_3 particles located on the AlN surface; a liquid phase is formed, which intensifies sintering at lower temperature [54].

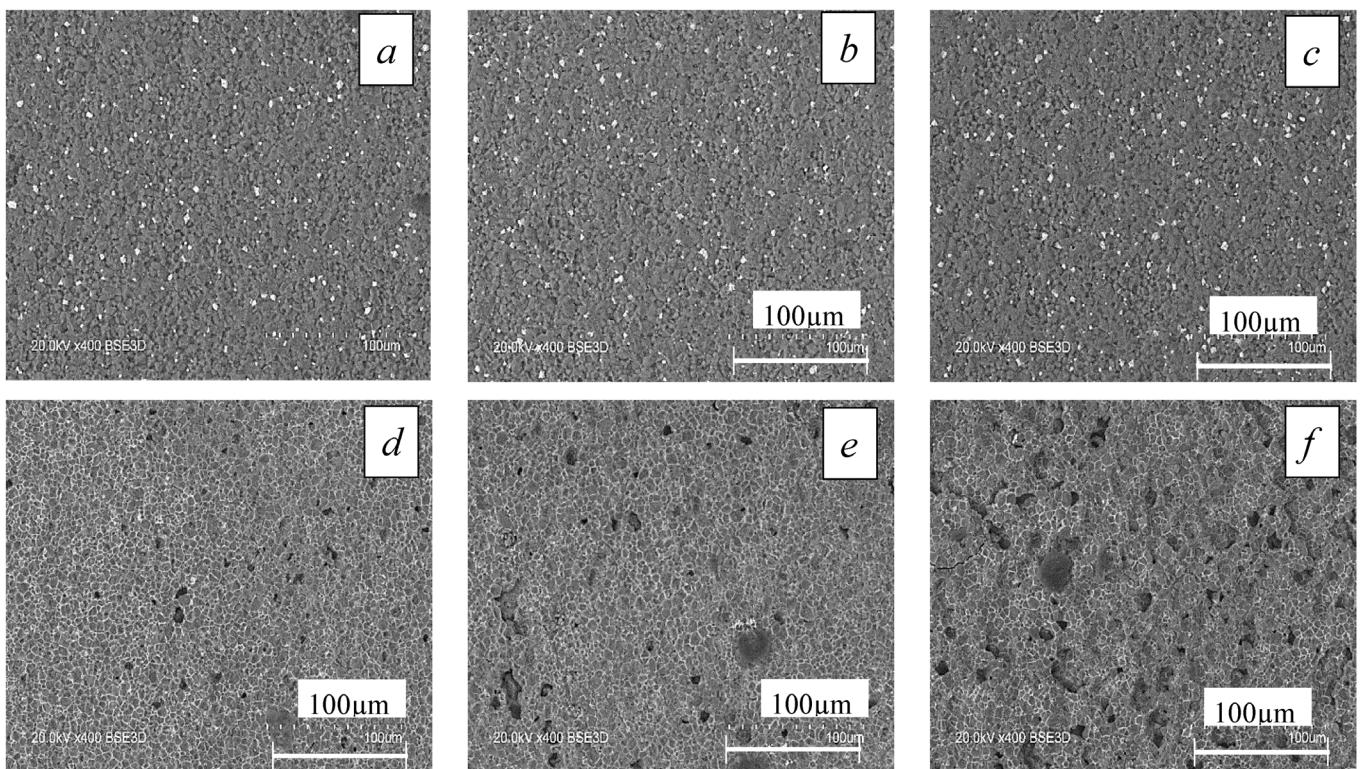


Figure 7. Surface of AlN samples processed at different temperatures: (a) original, (b) 1300 °C, (c) 1400 °C, (d) 1500 °C, (e) 1600 °C, (f) 1700 °C. The gray elements in the images are AlN grains. The bright areas are supposedly yttrium aluminate.

After treatment at a temperature of 1300–1400 °C, changes in surface morphology are barely discernible; however, this temperature is not high enough for the formation of visible grain boundaries compared to the previously shown aluminum oxide. Further increase in processing temperature to 1500 °C is accompanied by the formation of a distinct grain structure on the irradiated surface, as well as shallow pores up to 10 μm in size evenly scattered over the AlN surface. The average grain size of aluminum oxide is 10 μm, and the bright inclusions corresponding to yttrium no longer appear in the surface structure. Instead, thin veins containing predominantly oxygen and yttrium are formed on the grain boundaries. After the temperature rises to 1600 °C (Figure 7e), further transformation of the surface structure is observed, namely the absorption of small grains by larger ones, as

evidenced by an increase in grain size as well by a decrease in the number of grains. The pore size increases to 15–20 μm . After treatment at a temperature of 1700 $^{\circ}\text{C}$ (Figure 7f), significant irregularities appear on the ceramic surface and porosity continues to increase. Additionally, a well-formed aluminum–yttrium structure is seen on the surface, as in Figure 8.

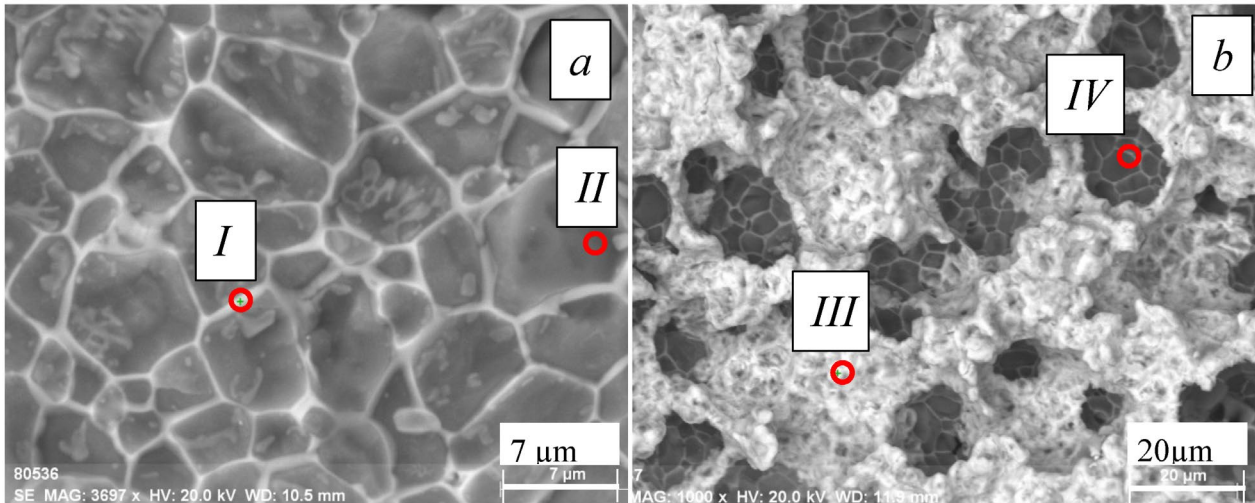


Figure 8. Formation of an aluminum–yttrium structure on the AlN surface processed at temperatures of 1500 $^{\circ}\text{C}$ (a) and 1700 $^{\circ}\text{C}$ (b).

The elemental composition measured at different areas in Figure 8 is summarized in Table 4. The areas (I, II, III, and IV) are enumerated according to Figure 8.

Table 4. Elemental composition of different regions of irradiated AlN ceramic, at%.

	Nitrogen	Oxygen	Aluminum	Yttrium
I	24.2	25.5	44.8	5.6
II	41.6	6.6	52.0	0.3
III	0	60.6	11.5	27.9
IV	0	21.4	65.8	12.0

A histogram of the elemental distribution is shown in Figure 9. As seen, regions I and II are characterized by low yttrium content. The content is minimum in region II, within the measurement accuracy. In region I, the yttrium content increases, and one can assume the formation of a third phase in the intergranular region. Region III has the highest yttrium content. The most probable mechanism responsible for the formation of high yttrium content is the high temperature in the processing region, which leads to the formation of an aluminum–yttrium structure through the reaction of yttrium with oxygen and nitrogen, yielding yttrium oxide Y_2O_3 and yttrium nitride YN , which, in turn interact with aluminum oxide Al_2O_3 to form this surface structure.

X-ray diffraction patterns of original and irradiated sample surfaces treated at temperatures of 1600 $^{\circ}\text{C}$ and 1700 $^{\circ}\text{C}$ are shown in Figure 10.

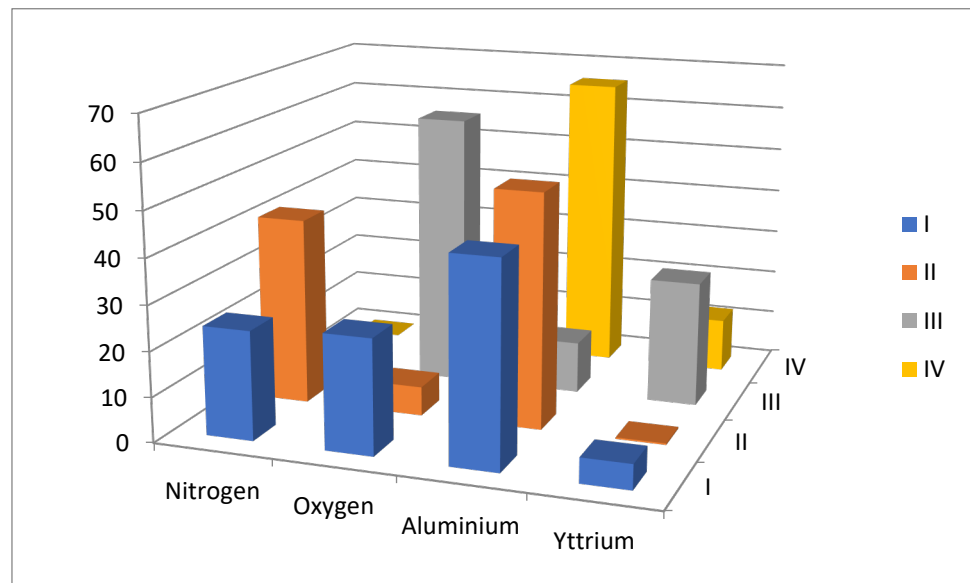


Figure 9. Histogram of elemental composition over the irradiated AlN surface. The isothermal holding temperature is 1700 °C.

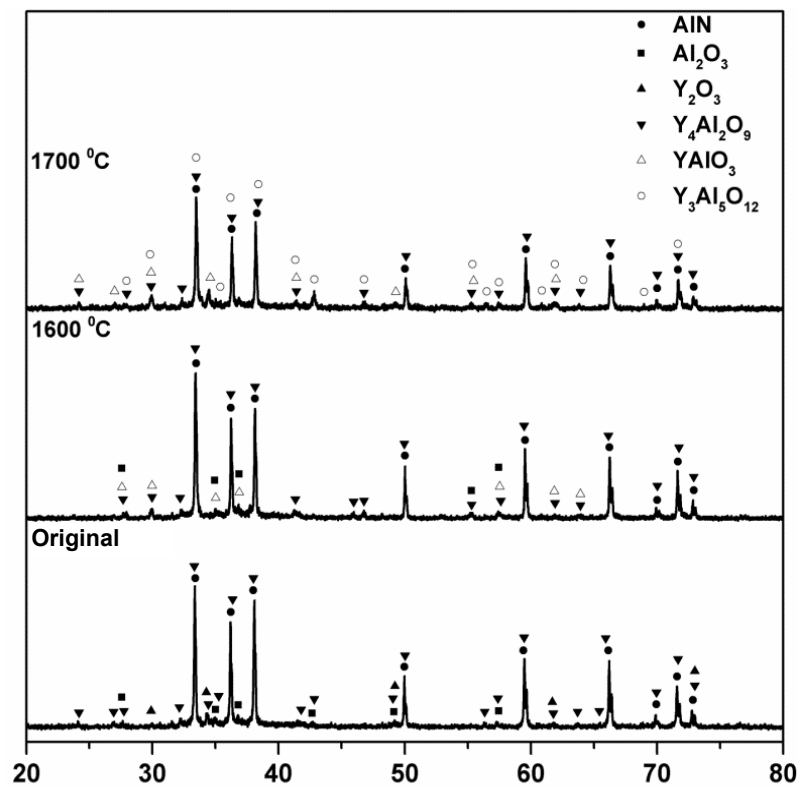
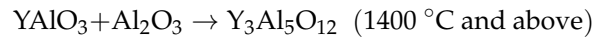
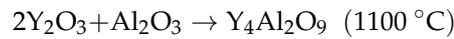


Figure 10. X-ray diffraction patterns of AlN + Y₂O₃ samples; original, and at temperatures of 1600 °C and 1700 °C.

X-ray diffraction analysis indicates that the AlN + Y₂O₃ samples consist predominantly of the AlN (P63mc (186)) phase. As seen from Figure 10, the original AlN + Y₂O₃ sample also includes phases of Al₂O₃ (R-3ch (167)), Y₂O₃ (F2/m-3 (202)), and Y₄Al₂O₉ (P121/c1 (14)). At a temperature of 1600 °C, the YAlO₃ (P63/mmc (194)) phase is formed, a result of interaction of Y₄Al₂O₉ and Al₂O₃. As the temperature increases further to 1700 °C, it is likely to form the Y₃Al₅O₁₂ (Ia-3d (230)) phase of the yttrium–aluminum garnet as a result

of reaction between $YAlO_3$ and Al_2O_3 [55,56]. Shown below are reactions for powders of the Al_2O_3 – Y_2O_3 system synthesized using the nanospray drying method [57]:



Thus, as the processing temperature increases, yttrium oxide first embeds in the grain boundaries as they are formed, and then rises to the surface to form an aluminum–yttrium structure, which may affect the strength and thermal properties.

Figure 11 shows the dependence of hardness, measured by the Vickers method, on processing temperature for aluminum nitride.

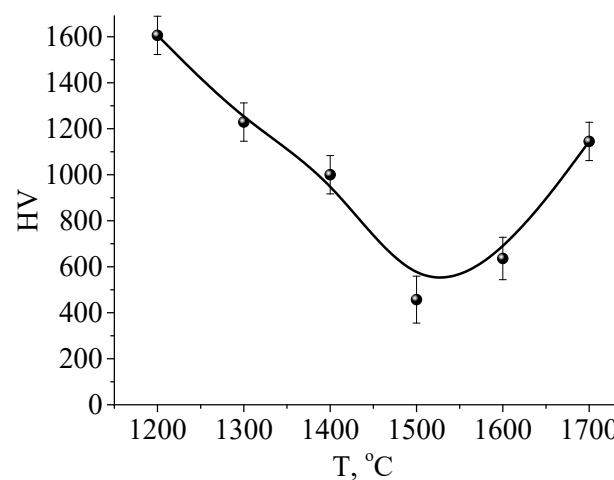


Figure 11. Dependence of AlN hardness measured by the Vickers method on processing temperature.

One can see from Figure 11 that the sample microhardness decreases as the processing temperature increases to 1500 °C. This decrease can be associated with the formation of a region with a broken structure in the surface layer and increased porosity of the material, which is indirectly confirmed by SEM images of the surface shown in Figure 7d–f. With further increase in temperature, along with an increase in the surface hardness due to the formation of the aluminum–yttrium structure, the hardness is improved due to the healing of small cracks and pores. However, the hardness increases but does not achieve the value of the original sample. A decrease in the hardness of high-density ceramics after irradiation by electrons and ions is a known effect [58], which is associated with cracking of the surface layer after processing. An increase in microhardness on account of surface layer melting has been observed previously only for porous ceramics [59], which were not a study subject of this work.

As with the aluminum oxide ceramic, roughness measurements for the aluminum nitride ceramic (Table 5) show an increasing temperature dependence. As seen from Table 5, this increase is not linear, but occurs in a stepwise manner.

At relatively low temperature of up to 1400 °C, the roughness varies within the measurement accuracy. However, at a temperature of 1500 °C, the roughness increases by more than a factor of four (the parameter R_a increases from 0.68 to 2.66 μm). This roughness dependence correlates with the microscopic data (Figure 7).

Table 5. Roughness measurements of AlN substrates after electron-beam processing at different temperatures.

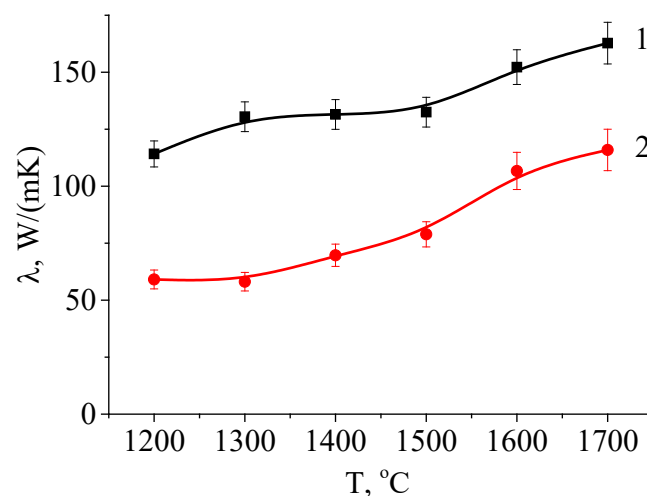
Processing Regime	R_a , μm
Original	0.671
1300 °C	0.754
1400 °C	0.679
1500 °C	2.656
1600 °C	2.581
1700 °C	3.795

4.4. Thermal Conductivity Measurement of the AlN Ceramic after Electron-Beam Processing

The high thermal conductivity of the aluminum nitride ceramic, along with its electrical insulating and strength properties in comparison with other types of ceramics and its non-toxicity, makes this material important to the electronics industry. The theoretical value of thermal conductivity of AlN, according to [60], can reach 320 W/(m·K); however, in practice, this value is limited for commercially available specimens by a great number of defects due to oxygen dissolved in the AlN lattice. According to [61–63], the mechanism of defect formation can be as follows: oxygen dissolved in the AlN (O_N) lattice induces the formation of aluminum atom vacancies (V_Al), and due to the considerable mass mismatch between these vacancies and the surrounding lattice, a defect with very large phonon scattering cross-section is created. The presence of oxygen in AlN is connected with its content in the original powder used for sintering. This content may amount to 1%.

As noted above, since AlN is a material with a covalent bond, it has a low diffusion coefficient, and this requires high sintering temperatures (>1600 °C). Moreover, in the presence of protective oxide on the surface and oxygen in the crystal lattice, it is impossible to reach high thermal conductivity without using sintering additives. The role of additives is to form a liquid phase by interacting with the oxide layer (Al_2O_3) on the surface of compacted particles and to act as a “sink” to remove oxygen from the lattice [64]. Other methods of achieving high thermal conductivity include sintering at temperatures above 1800 °C for several hours, irradiation by high-energy neutrons [65], and heat treatment after sintering in various reducing atmospheres at high temperature [66–69]. In the work described here, for heat treatment we used electron-beam irradiation in residual atmosphere at a chamber pressure of 10 Pa.

Figure 12 shows the thermal conductivity of AlN ceramic after irradiation at different temperatures.

**Figure 12.** Dependence of thermal conductivity on processing temperature. The temperature at which the measurements were carried out: 1—50 °C, 2—500 °C.

Increase in the isothermal holding temperature leads to an increase in thermal conductivity, with the largest change observed for samples sintered at 1500 °C and above, at which temperature an aluminum–yttrium structure is formed on the surface. Despite increase in surface roughness and decrease in strength, thermal conductivity increases with the formation of pores. This effect can be related to an increase in the size of ceramic grains with simultaneous decrease in their number. Decrease in phonon scattering on grain boundaries is apparently a factor that facilitates the increase in thermal conductivity.

4.5. Effect of Electron-Beam Processing on Ceramic Wettability

The contact wetting angle determines the degree of interaction between a liquid and a solid surface and characterizes its moisture resistance, anti-corrosion, anti-bacterial, and other properties. Depending on the purpose and conditions of applications, it may be advantageous to either increase or decrease the contact angle [70–72]. The contact angle depends on interfacial surface energies of the liquid, solid, and gaseous states, as well as on the surface roughness and chemical composition. There are several methods of changing the contact angle, such as physical or chemical modification of the surface, application of coatings, creation of structures with various geometry and size, and others. [73,74]. In the present work we have explored the effect of electron-beam irradiation on surface properties and contact angle.

As noted above, the roughness increases after electron-beam processing, which in general should result in a decrease in the contact angle compared to the smooth surface, provided the same interfacial surface energies. This effect arises due to increase in contact area with the liquid and more possibilities for the formation of molecular bonds. However, in certain cases, the roughness can lead to an increase in contact angle due to the formation of air cavities between surface irregularities. This phenomenon is called composite wetting and can be used to create super hydrophobic surfaces with contact angle over 150° [75].

Figures 13 and 14 show photographs of the original and processed substrate surfaces of aluminum oxide and aluminum nitride taken after processing at different temperatures. One can see that the droplets on the irradiated surface for both ceramics are larger than on the non-irradiated surface.

Table 6 shows the results of measurements of contact wetting angle for the substrates under study.

Table 6. Measured contact wetting angle.

Processing Regime	Al ₂ O ₃	INC-AN180
Original	63°	56°
1300 °C	53°	93°
1400 °C	97°	20°
1500 °C	98°	38°
1600 °C	88°	73°
1700 °C	94°	101°

The data in Table 6 are charted in Figure 15. As can be seen, with increase in irradiation temperature, the contact angle varies differently for oxide and nitride ceramics. Thus, for Al₂O₃ samples treated at 1400 °C and above the surface wettability decreases. The ceramic surface exhibits hydrophobic properties, which is manifested by an increase in contact angle from 63° for the untreated surface to 90°–100° for the irradiated surface. The wettability dependence for AlN ceramic is nonmonotonic. At low processing temperature, the wettability decreases noticeably, then at a temperature of 1400 °C the contact angle abruptly decreases, and the surface acquires more hydrophobic properties: the contact angle decreases by more than a factor of two. With further increase in processing temperature, the contact angle increases, exceeding 100°.

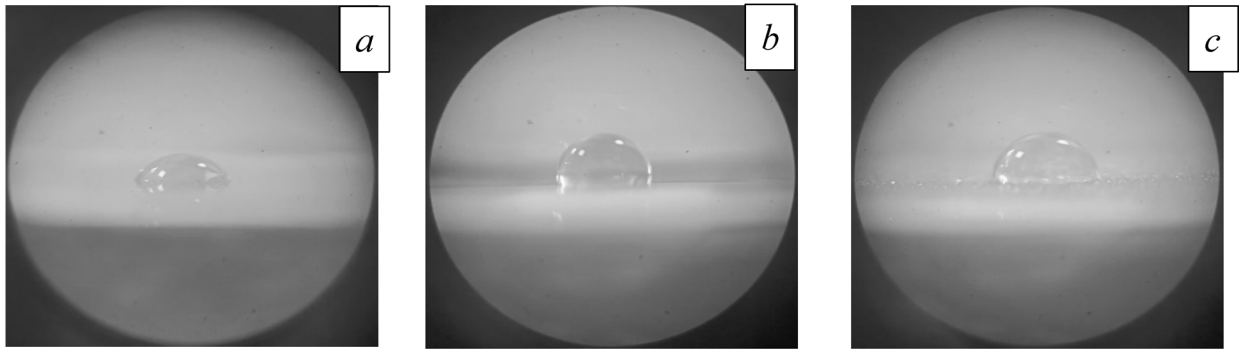


Figure 13. Photographs of water droplets on the surface of Al₂O₃ substrates: (a) original sample; (b) after processing at a temperature of 1600 °C; (c) after processing at a temperature of 1700 °C.

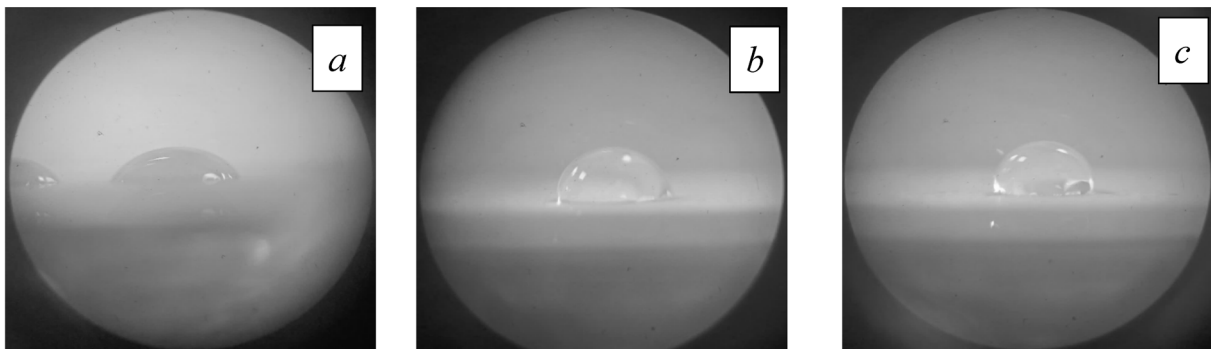


Figure 14. Photographs of water droplets on the surface of AlN substrates: (a) original sample; (b) after processing at a temperature of 1600 °C; (c) after processing at a temperature of 1700 °C.

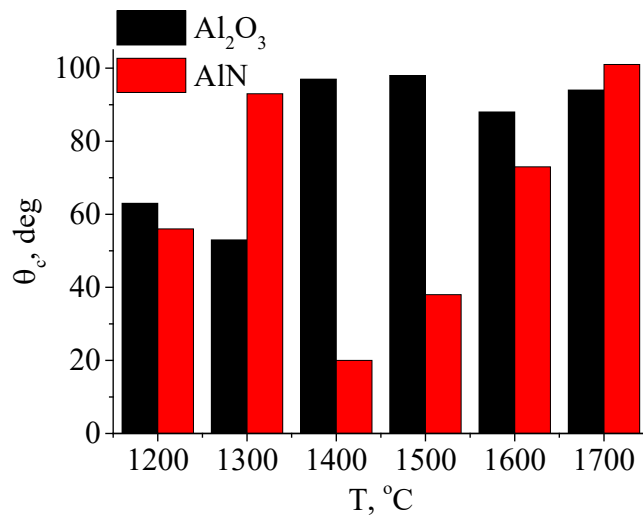


Figure 15. Contact angles of Al₂O₃ and AlN surfaces. A temperature of 1200 °C corresponds to non-irradiated material.

The contact angle is determined by the interaction between molecules of the liquid and the solid surface. A lower contact angle indicates that the solid body has lower surface energy; the energy increases with increasing processing temperature. According to [76], the observed increase in hydrophilicity can be related to increase in surface roughness, as in the case of irradiation by a femtosecond laser [77]. Note also another possible mechanism is related to change in the chemical composition of the irradiated surface. After electron-beam processing the content of Al on the surface of AlN substrate increases (according to Table 4 and Figure 10). A thin layer of aluminum oxide is formed due to oxidation. However, a

large number of Al^{3+} and O^{2-} ions produced by electron-beam irradiation do not combine immediately, resulting in the formation of a Lewis acid and base pair, which expands the polar areas on the surface and improves the surface energy and hydrophilicity [78–80].

5. Conclusions

Electron-beam irradiation of aluminum-containing ceramics Al_2O_3 and AlN by a plasma-cathode electron source in the forevacuum pressure range provides an effective method of surface modification of these ceramic materials.

Small changes in the surface properties begin to appear when the processing temperature reaches about 1500 °C. From this temperature and further as the temperature increases, the surface of the ceramic begins to show the effects of melting and re-crystallization, which result in grain growth on the surface of Al_2O_3 , and, in the case of irradiation of AlN, the formation of aluminum nitride structures.

The microhardness and roughness of the irradiated ceramic surface increases with increasing processing temperature. The contact wetting angle of the AlN surface can vary from 20° to 100° depending on temperature, which allows one to control the transition of the material from hydrophilic to hydrophobic. Electron-beam irradiation of Al_2O_3 does not affect the wettability of this material to such an extent.

The thermal conductivity of ceramic substrates subjected to electron-beam treatment in the forevacuum pressure range increases by a factor of 1.5 to 2 over the untreated surface, which is connected to increase in the size of ceramic grains and simultaneous decrease in their number. A decrease in phonon scattering on grain boundaries facilitates an increase in thermal conductivity.

The results of the work described here contribute to the further development of technologies for electron-beam modification of ceramic materials.

Author Contributions: Conceptualization, A.K.; validation, A.K., I.B. and A.Z.; formal analysis, A.Z.; investigation, A.K.; resources, A.Z.; writing—original draft preparation, A.K.; writing—review and editing, I.B.; project administration, A.K.; funding acquisition, A.K. All authors have read and agreed to the published version of the manuscript.

Funding: This work was supported by the Ministry of Science and Higher Education of the Russian Federation. Grant FEWM-2021-0013.

Institutional Review Board Statement: Not applicable.

Informed Consent Statement: Not applicable.

Acknowledgments: Special thanks to Ian Brown (Berkeley Lab) for English correction and helpful discussion.

Conflicts of Interest: The authors declare no conflict of interest. The funders had no role in the design of the study; in the collection, analyses, or interpretation of data; in the writing of the manuscript; or in the decision to publish the results.

References

1. Baik, Y.; Drew, R.A. Aluminum nitride: Processing and applications. *Key Eng. Mater.* **1996**, *122*, 553. [[CrossRef](#)]
2. Werdecker, W.; Aldinger, F. Aluminum nitride—an alternative ceramic substrate for high power applications in microcircuits. *IEEE Trans. Compon. Hybrids Manuf. Technol.* **1984**, *7*, 399–404. [[CrossRef](#)]
3. Taylor, K.M.; Lenie, C. Some properties of aluminum nitride. *J. Electrochem. Soc.* **1960**, *107*, 308. [[CrossRef](#)]
4. Ivanov, S.N.; Popov, P.A.; Egorov, G.V. Thermophysical properties of ceramic aluminum nitride. *Phys. Solids* **1997**, *39*, 93–96. [[CrossRef](#)]
5. Abyzov, A.M. Aluminum oxide and alumina ceramics (review). Part 1. Properties of Al_2O_3 and commercial production of dispersed Al_2O_3 . *Refract. Ind. Ceram.* **2019**, *60*, 24–32. [[CrossRef](#)]
6. Figiel, P.; Rozmus, M.; Smuk, B. Properties of alumina ceramics obtained by conventional and non-conventional methods for sintering ceramics. *J. Achiev. Mater. Manuf. Eng.* **2011**, *48*, 29–34.
7. Parikh, P.B. Alumina ceramics: Engineering applications and domestic market potential. *Trans. Indian Ceram. Soc.* **1995**, *54*, 179–184. [[CrossRef](#)]

8. Dalla Pria, P. Evolution and new application of the alumina ceramics in joint replacement. *Eur. J. Orthop. Surg. Traumatol.* **2007**, *17*, 253–256. [[CrossRef](#)]
9. Kim, J.I.; Kim, J.; Lee, S.M.; Jeong, H.; Ryu, S.S. Low-temperature hot-press sintering of AlN ceramics with MgO–CaO–Al₂O₃–SiO₂ glass additives for ceramic heater applications. *Ceram. Int.* **2022**, *48*, 26022–26027. [[CrossRef](#)]
10. Fiedler, H.; Leveneur, J.; Kennedy, J. Advanced AlN ceramic materials for energy-efficient communication devices. In *Advanced Ceramics for Energy Storage, Thermoelectrics and Photonics*; Elsevier: Amsterdam, The Netherlands, 2023; pp. 237–255.
11. Ruppi, S.; Larsson, A. Chemical vapour deposition of k-Al₂O₃. *Thin Solid Film* **2001**, *388*, 50–61. [[CrossRef](#)]
12. Pradhan, S.K.; Reucroft, P.J.; Ko, Y. Crystallinity of Al₂O₃ films deposited by metalorganic chemical vapor deposition. *Surf. Coat. Technol.* **2004**, *176*, 382–384. [[CrossRef](#)]
13. Kawakami, N.; Yokota, Y.; Tachibana, T.; Hayashi, K.; Kobashi, K. Atomic layer deposition of Al₂O₃ thin films on diamond. *Diam. Relat. Mater.* **2005**, *14*, 2015–2018. [[CrossRef](#)]
14. Zhang, Y.; Bertrand, J.A.; Yang, R.; George, S.M.; Lee, Y.C. Electroplating to visualize defects in Al₂O₃ thin films grown using atomic layer deposition. *Thin Solid Film.* **2009**, *517*, 3269–3272. [[CrossRef](#)]
15. Guo, J.; Sun, Y.; Qiu, T.; Xue, W.; Yang, H. Gelating and drying process of aqueous gelcasting aluminum nitride ceramics. *Int. J. Appl. Ceram. Technol.* **2015**, *12*, E23–E32. [[CrossRef](#)]
16. Gottmann, J.; Kreutz, E.W. Pulse laser deposition of alumina and zirconia thin films on polymers and glass as optical and protective coating. *Surf. Coat. Technol.* **1999**, *116*, 1189–1194. [[CrossRef](#)]
17. Jing, C.; Zhao, X.; Zhang, Y. Sol–gel fabrication of compact, crack-free alumina film. *Mater. Res. Bull.* **2007**, *42*, 600–608. [[CrossRef](#)]
18. Masalski, J.; Gluszek, J.; Zabrzanski, J.; Nitsch, K.; Gluszek, P. Improvement in corrosion resistance of the 316l stainless steel by means of Al₂O₃ coatings deposited by the sol-gel method. *Thin Solid Film* **1999**, *349*, 186–190. [[CrossRef](#)]
19. Sun, R.; Yang, X.; Arima, K.; Kawai, K.; Yamamura, K. High-quality plasma-assisted polishing of aluminum nitride ceramic. *CIRP Ann.* **2020**, *69*, 301–304. [[CrossRef](#)]
20. Dukenbayev, K.; Kozlovskiy, A.; Korolkov, I.; Zdorovets, M. Investigation of radiation resistance of AlN ceramics. *Vacuum* **2019**, *159*, 144–151. [[CrossRef](#)]
21. Lysenko, E.N.; Vlasov, V.A.; Malyshev, A.V.; Surzhikov, A.P. Structural and magnetic properties of lithium-substituted ferrite ceramics sintered by continuous electron beam heating. *Nucl. Instrum. Methods Phys. Res. Sect. B Beam Interact. Mater. At.* **2020**, *470*, 28–31. [[CrossRef](#)]
22. Karansky, V.V.; Klimov, A.S.; Smirnov, S.V. Structural transformations in Mn–Zn ferrite under low-energy electron beam treatment. *Vacuum* **2020**, *173*, 109115. [[CrossRef](#)]
23. Mirzayev, M.N.; Popov, E.; Demir, E.; Abdurakhimov, B.A.; Mirzayeva, D.M.; Sukratov, V.A.; Kristavchuk, O. Thermophysical behavior of boron nitride and boron trioxide ceramics compounds with high energy electron fluence and swift heavy ion irradiated. *J. Alloys Compd.* **2020**, *834*, 155119. [[CrossRef](#)]
24. Zhang, X.; Chen, N.; Wu, J.; Wei, J.; Yan, B.; Li, L.; He, N. Rapid fabrication of surface microstructures on AlN HTCC substrate by chemically assisted laser ablation. *Ceram. Int.* **2021**, *47*, 27598–27608. [[CrossRef](#)]
25. Stolz, B.; Poprawe, R. Surface conductivity modification of ceramics with laser radiation. *Surf. Coat. Technol.* **1999**, *112*, 394–400. [[CrossRef](#)]
26. Egashira, Y.; Kim, H.; Komiyama, H. Cluster Size Determination in the Chemical Vapor Deposition of Aluminum Nitride. *J. Am. Ceram. Soc.* **1994**, *8*, 2009–2016. [[CrossRef](#)]
27. Schünemann, F.H.; Galárraga-Vinueza, M.E.; Magini, R.; Fredel, M.; Silva, F.; Souza, J.C.; Henriques, B. Zirconia surface modifications for implant dentistry. *Mater. Sci. Eng. C* **2019**, *98*, 1294–1305. [[CrossRef](#)]
28. Ivanov, K.V.; Chesnokov, A.E.; Smirnov, A.V. Application of high current pulsed electron beam irradiation to smoothing of cold spray aluminum bronze coating. *Vacuum* **2022**, *197*, 110780. [[CrossRef](#)]
29. Sabet, M.; Hassan, A.; Ratnam, C.T. Mechanical, electrical, and thermal properties of irradiated low-density polyethylene by electron beam. *Polym. Bull.* **2020**, *68*, 2323–2339. [[CrossRef](#)]
30. Stankova, N.E.; Atanasov, P.A.; Nikov, R.G.; Nikov, R.G.; Nedyalkov, N.N.; Stoyanchoy, T.R.; Fukata, N.; Kolev, K.N.; Valova, E.I.; Georgieva, J.S.; et al. Optical properties of polydimethylsiloxane (PDMS) during nanosecond laser processing. *Surf. Sci.* **2016**, *374*, 96–103. [[CrossRef](#)]
31. Kumar, R.; Khan, M.W.; Srivastava, J.P.; Arora, S.K.; Sofin, R.G.S.; Choudhary, R.J.; Shvets, I.V. Swift heavy ion irradiation-induced modifications in structural, magnetic and electrical transport properties of epitaxial magnetic thin films. *J. Appl. Phys.* **2006**, *100*, 033703. [[CrossRef](#)]
32. Sreedevi, A.; Priyanka, K.P.; Babitha, K.K.; Ganesh, S.; Varghese, T. Influence of electron beam irradiation on structural and optical properties of α -Ag₂WO₄ nanoparticles. *Micron* **2016**, *88*, 1–6.
33. Onoe, J.; Nakayama, T.; Aono, M.; Hara, T. Structural and electrical properties of an electron-beam-irradiated C60 film. *Appl. Phys. Lett.* **2003**, *4*, 595–597. [[CrossRef](#)]
34. Yasuda, K.; Kinoshita, C. Electron-beam induced dissociation of dislocation loops in magnesia–alumina ceramics. *Nucl. Instrum. Methods Phys. Res. Sect. B Beam Interact. Mater. At.* **2002**, *191*, 559–564. [[CrossRef](#)]
35. Burdovitsin, V.A.; Dvilis, E.S.; Medovnik, A.V.; Oks, E.M.; Khasanov, O.L.; Yushkov, Y.G. Surface structure of alumina ceramics during irradiation by a pulsed electron beam. *Tech. Phys.* **2013**, *58*, 111–113. [[CrossRef](#)]

36. Bakeev, I.Y.; Dvilis, E.S.; Klimov, A.S.; Oks, E.M.; Zenin, A.A. The possibilities of dimensional electron-beam processing as applied to selective sintering of oxide ceramics in the forevacuum pressure range. *J. Phys. Conf. Ser.* **2018**, *945*, 012016. [[CrossRef](#)]
37. Surzhikov, A.P.; Frangulyan, T.S.; Ghyngazov, S.A.; Vasiliev, I.P. Electron microscopy studies of near-surface layers of ZrO₂(Y)-Al₂O₃ composite ceramic modified by high-current beam of low-energy electrons. *Inorg. Mater. Appl. Res.* **2014**, *5*, 536–539. [[CrossRef](#)]
38. Burdovitsin, V.A.; Klimov, A.S.; Medovnik, A.V.; Oks, E.M. Electron beam treatment of non-conducting materials by a fore-pump-pressure plasma-cathode electron beam source. *Plasma Sources Sci. Technol.* **2010**, *19*, 055003. [[CrossRef](#)]
39. Klimov, A.S.; Bakeev, I.Y.; Dvilis, E.S.; Oks, E.M.; Zenin, A.A. Electron beam sintering of ceramics for additive manufacturing. *Vacuum* **2019**, *169*, 108933. [[CrossRef](#)]
40. Klimov, A.S.; Bakeev, I.Y.; Oks, E.M.; Zenin, A.A. Electron-beam sintering of an Al₂O₃/Ti composite using a forevacuum plasma-cathode electron source. *Ceram. Int.* **2020**, *46*, 22276–22281. [[CrossRef](#)]
41. Klimov, A.S.; Zenin, A.A.; Bakeev, I.Y.; Oks, E.M. Formation of gradient metaloceramic materials using electron-beam irradiation in the forevacuum. *Russ. Phys. J.* **2019**, *62*, 1123–1129. [[CrossRef](#)]
42. Ivanova, A.S. Aluminum oxide and systems based on it: Properties and applications. *Kinet. Catal.* **2012**, *53*, 425–439. [[CrossRef](#)]
43. Miyashiro, F.; Iwase, N.; Tsuge, A.; Ueno, F.; Nakahashi, M.; Takahashi, T. High thermal conductivity aluminum nitride ceramic substrates and packages. *IEEE Transactions on Components, Hybrids Manuf. Technol.* **1990**, *13*, 313–319. [[CrossRef](#)]
44. Jackson, T.B.; Virkar, A.V.; More, K.L.; Dinwiddie, R.B., Jr.; Cutler, R.A. High-thermal-conductivity aluminum nitride ceramics: The effect of thermodynamic, Kinetic, and microstructural factors. *J. Am. Ceram. Soc.* **1997**, *80*, 1421–1435. [[CrossRef](#)]
45. Miroshkin, V.P.; Panova, Y.I.; Pasyukov, V.V. Dielectric relaxation in polycrystalline ferrites. *Phys. Stat. Sol. A* **1981**, *66*, 779–782. [[CrossRef](#)]
46. Kwok, D.Y.; Neumann, A.W. Contact angle measurement and contact angle interpretation. *Adv. Colloid Interface Sci.* **1999**, *81*, 167–249. [[CrossRef](#)]
47. Klimov, A.; Bakeev, I.; Oks, E.; Zenin, A. Forevacuum plasma source of continuous electron beam. *Laser Part. Beams* **2019**, *37*, 203–208. [[CrossRef](#)]
48. Sarkar, R. *Refractory Technology: Fundamentals and Applications*; CRC Press: Boca Raton, FL, USA, 2023.
49. Ansell, S.; Krishnan, S.; Weber, J.R.; Felten, J.J.; Nordine, P.C.; Beno, M.A.; Saboungi, M.L. Structure of liquid aluminum oxide. *Phys. Rev. Lett.* **1997**, *78*, 464. [[CrossRef](#)]
50. San Miguel, M.A.; Sanz, J.F.; Alvarez, L.J.; Odriozola, J.A. Molecular-dynamics simulations of liquid aluminum oxide. *Phys. Rev. B* **1998**, *58*, 2369. [[CrossRef](#)]
51. Bitjukov, V.K.; Petrov, V.A. Absorption coefficient of molten aluminum oxide in semitransparent spectral range. *Appl. Phys. Res.* **2013**, *5*, 51. [[CrossRef](#)]
52. Maslyayev, S.A.; Morozov, E.V.; Romakhin, P.A.; Pimenov, V.N.; Gribkov, V.A.; Tikhonov, A.N.; Bondarenko, G.G.; Dubrovsky, A.V.; Kazilin, E.E.; Sasinovskaya, I.P.; et al. Damage of Al₂O₃ ceramics under the action of pulsed ion and plasma fluxes and laser irradiation. *Inorg. Mater. Appl. Res.* **2016**, *7*, 330–339. [[CrossRef](#)]
53. Lee, H.M.; Bharathi, K.; Kim, D.K. Processing and characterization of aluminum nitride ceramics for high thermal conductivity. *Adv. Eng. Mater.* **2014**, *16*, 655–669. [[CrossRef](#)]
54. Harris, J.H. Sintered aluminum nitride ceramics for high-power electronic applications. *JOM* **1998**, *50*, 56–60. [[CrossRef](#)]
55. Muradyan, G.N.; Dolukhanyan, S.K.; Aleksanyan, A.G.; Ter-Galstyan, O.P.; Mnatsakanyan, N.L. Regularities and Mechanism of Formation of Aluminides in the TiH₂-ZrH₂-Al System. *Russ. J. Phys. Chem. B* **2019**, *13*, 86–95. [[CrossRef](#)]
56. Hlavac, J. Melting temperatures of refractory oxides: Part I. *Pure Appl. Chem.* **1982**, *54*, 681–688. [[CrossRef](#)]
57. Paigin, V.D.; Deulina, D.E.; Ileva, A.E.; Lyamina, G.V.; Dvilis, E.S.; Valiev, D.T.; Stepanov, S.A.; Khasanov, O.L.; Ditts, A.A. Synthesis and Investigation of the Properties of Al₂O₃-Y₂O₃ Powders Using Nanospray Drying. *Rev. Adv. Chem.* **2022**, *12*, 270–276. [[CrossRef](#)]
58. Pu, G.; Zou, J.; Lin, L.; Zhang, K.; Liu, B.; Ma, F.; Wang, Q.; Li, Q. Effects of He ion irradiation on the microstructures and mechanical properties of t' phase yttria-stabilized zirconia ceramics. *J. Alloys Compd.* **2019**, *771*, 777–783. [[CrossRef](#)]
59. Ghyngazov, S.A. Zirconia ceramics processing by intense electron and ion beams. *Nucl. Instrum. Methods Phys. Res. Sect. B Beam Interact. Mater. At.* **2018**, *435*, 190–193. [[CrossRef](#)]
60. Slack, G.A.; Tanzilli, R.A.; Pohl, R.O.; Vandersande, J.W. The intrinsic thermal conductivity of AlN. *J. Phys. Chem. Solids* **1987**, *48*, 641–647. [[CrossRef](#)]
61. Slack, G.A.; McNelly, T.F. Growth of high purity AlN crystals. *J. Cryst. Growth* **1976**, *34*, 263–279. [[CrossRef](#)]
62. Slack, G.A.; Tanzilli, R.A. Pohl RO and Vandersande JW. *J. Phys. Chem. Solids* **1987**, *1987*, 48.
63. Slack, G.A. Nonmetallic crystals with high thermal conductivity. *J. Phys. Chem. Solids* **1973**, *34*, 321–335. [[CrossRef](#)]
64. Virkar, A.V.; Jackson, T.B.; Cutler, R.A. Thermodynamic and kinetic effects of oxygen removal on the thermal conductivity of aluminum nitride. *J. Am. Ceram. Soc.* **1989**, *72*, 2031–2042. [[CrossRef](#)]
65. Yano, T.; Iseki, T. Thermal and mechanical properties of neutron-irradiated aluminum nitride. *J. Nucl. Mater.* **1991**, *179*, 387–390. [[CrossRef](#)]
66. Watari, K.; Kawamoto, M.; Ishizaki, K. Sintering chemical reactions to increase thermal conductivity of aluminium nitride. *J. Mater. Sci.* **1991**, *26*, 4727–4732. [[CrossRef](#)]
67. Fujimoto, M.; Ueda, S. Effect of annealing in CF₄ gas atmosphere on thermal conductivity of AlN ceramics. *J. Ceram. Soc. Jpn.* **1988**, *96*, 1210–1213. [[CrossRef](#)]

68. Kasori, M.; Ueno, F.; Tsuge, A. Effects of Transition-Metal Additions on the Properties of AlN. *J. Am. Ceram. Soc.* **1994**, *77*, 1991–2000. [[CrossRef](#)]
69. Hirano, M.; Kato, K.; Isobe, T.; Hirano, T. Sintering and characterization of fully dense aluminium nitride ceramics. *J. Mater. Sci.* **1993**, *28*, 4725–4730. [[CrossRef](#)]
70. Zhao, Y.-P. *Characterization of Amorphous and Crystalline Rough Surface: Principles and Applications*; Elsevier: San Diego, CA, USA, 2000.
71. Foadi, F.; Brink, G.H.T.; Mohammadizadeh, M.R.; Palasantzas, G. Roughness dependent wettability of sputtered copper thin films: The effect of the local surface slope. *J. Appl. Phys.* **2019**, *125*, 244307. [[CrossRef](#)]
72. Zhang, Y. The Effect of Surface Roughness Parameters on Contact and Wettability of Solid Surfaces. Ph.D. Thesis, Iowa State University, Ames, IA, USA, 2007.
73. Lai, L.; Irene, E.A. Area evaluation of microscopically rough surfaces. *J. Vac. Sci. Technol. B Microelectron. Nanometer Struct. Process. Meas. Phenom.* **1999**, *17*, 33–39. [[CrossRef](#)]
74. Croll, S.G. Surface roughness profile and its effect on coating adhesion and corrosion protection: A review. *Prog. Org. Coat.* **2020**, *148*, 105847. [[CrossRef](#)]
75. Parvate, S.; Dixit, P.; Chattopadhyay, S. Superhydrophobic surfaces: Insights from theory and experiment. *J. Phys. Chem. B* **2020**, *124*, 1323–1360. [[CrossRef](#)] [[PubMed](#)]
76. Wenzel, R.N. Resistance of solid surfaces to wetting by water. *Ind. Eng. Chem.* **2002**, *28*, 988–994. [[CrossRef](#)]
77. Yang, Q.; Lv, Z.; Cai, Y.; Cheng, J.; Lou, D.; Chen, L.; Liu, D. Femtosecond laser processing of AlN ceramics for gradient wettability control. *ECS J. Solid State Sci. Technol.* **2020**, *9*, 123010. [[CrossRef](#)]
78. Niu, C.N.; Han, J.Y.; Hu, S.P.; Chao, D.Y.; Song, X.G.; Howlader, M.M.R.; Cao, J. Fast and environmentally friendly fabrication of superhydrophilic-superhydrophobic patterned aluminum surfaces. *Surf. Interfaces* **2021**, *22*, 100830. [[CrossRef](#)]
79. Vidhya, Y.E.B.; Pattamatta, A.; Manivannan, A.; Vasa, N.J. Influence of fluence, beam overlap and aging on the wettability of pulsed Nd³⁺: YAG nanosecond laser-textured Cu and Al sheets. *Appl. Surf. Sci.* **2021**, *548*, 149259. [[CrossRef](#)]
80. Cardoso, J.T.; Garcia-Girón, A.; Huerta-Murillo, D.; Jagdheesh, R.; Walker, M.; Dimov, S.S.; Ocaña, J.L. Influence of ambient conditions on the evolution of wettability properties of an IR-, ns-laser textured aluminium alloy. *RSC Adv.* **2017**, *7*, 39617. [[CrossRef](#)]

Disclaimer/Publisher's Note: The statements, opinions and data contained in all publications are solely those of the individual author(s) and contributor(s) and not of MDPI and/or the editor(s). MDPI and/or the editor(s) disclaim responsibility for any injury to people or property resulting from any ideas, methods, instructions or products referred to in the content.